Assessing the wavelength extensibility of optical patterned defect inspection

Bryan M. Barnes*, Hui Zhou, Mark-Alexander Henn, Martin Y. Sohn, and Richard M. Silver
Engineering Physics Division, National Institute of Standards and Technology,
100 Bureau Drive MS 8212, Gaithersburg, MD, USA 20899-8212

ABSTRACT

Qualitative comparisons have been made in the literature between the scattering off deep-subwavelength-sized defects and the scattering off spheres in free space to illustrate the challenges of optical defect inspection with decreasing patterning sizes. The intensity scattered by such a sphere (for diameters sized well below the wavelength) is proportional to its diameter to the sixth power, but also scales inversely to the fourth power of the wavelength. This paper addresses through simulation the potential advantages of applying shorter wavelengths for improved patterned defect inspection. Rigorous finite-difference time-domain 3-D electromagnetic modeling of the scattering from patterned defect layouts has been performed at five wavelengths which span the deep ultraviolet (193 nm), the vacuum ultraviolet (157 nm and 122 nm), and the extreme ultraviolet (47 nm and 13 nm). These patterned structures and defects are based upon publicly disclosed geometrical cross-sectional information from recent manufacturing processes, which then have been scaled down to an 8 nm Si linewidth. Simulations are performed under an assumption that these wavelengths have the same source intensity, noise sources, and optical configuration, but wavelength-dependent optical constants are considered, thus yielding a more fundamental comparison of the potential gains from wavelength scaling. To make these results more practical, future work should include simulations with more process stacks and with more materials as well as the incorporation of available source strengths, known microscope configurations, and detector quantum efficiencies. In this study, a 47 nm wavelength yielded enhancements in the signal-to-noise by a factor of five compared to longer wavelengths and in the differential intensities by as much as three orders-of-magnitude compared to 13 nm, the actinic wavelength for EUV semiconductor manufacturing.

Keywords: defect metrology, extreme ultraviolet, EUV, vacuum ultraviolet, VUV, deep ultraviolet, DUV, defect inspection, finite-difference time-domain, simulation, simulated imaging

1. INTRODUCTION

A core principle of optical patterned defect inspection is that with decreased dimensions, "killer" pattered defects also scale in size proportionally [1-3]. A heuristic comparison has been made in the literature [3] between the scattering off deep-subwavelength-sized defects and the scattering off spheres in free space, the latter of which can be analytically solved using Mie's Theory [4]. This theory reduces to the Rayleigh approximation for a particle with diameter $d \ll \lambda$, the inspection wavelength, such that the scattered intensity I is given by

$$I = \left(\frac{1+cos^2\theta}{2R^2}\right)\left(\frac{2\pi}{\lambda}\right)^4\left(\frac{|\tilde{n}|^2-1}{|\tilde{n}|^2+2}\right)^2\left(\frac{d}{2}\right)^6 I_0 \quad \text{for } d \ll \lambda, \tag{1}$$

where $\tilde{n}$ is the complex index of refraction ($\tilde{n} = n + i\,k$), θ is the angle of incidence, R is the distance of the observer from the sphere, and I_0 is the incident intensity. Figure 1 illustrates the exponential decrease in scattered intensity for reduced diameters below 50 nm and the exponential increase in scattered intensity for reduced wavelengths shorter than 200 nm. Each plot in Fig. 1 optimistically assumes that no other variables in the scattering calculation in Eqn. 1 change except for a single parameter of interest.

Although Eqn. 1 may suggest trends for the intensities scattered by a defect, there are several key caveats. First, if the wavelength is scaled down such that $d \cong \lambda$ then Eqn. 1 is no longer valid and the full Mie Theory would be required. Second, even if $d \gg \lambda$, one must also consider variations in the index of refraction. The d^6 trend shown in Fig. 1 would be mostly unaffected except for the very smallest diameters, as it has been shown that nanoparticles with

*bryan.barnes@nist.gov; phone 1 301 975-3947; fax 1 301 975-4396; www.nist.gov

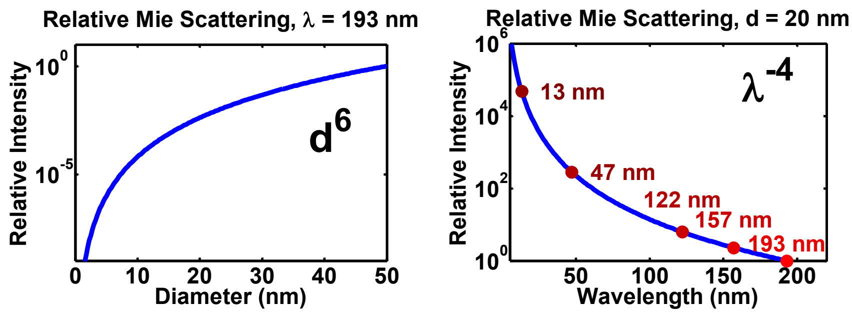

Figure 1. Trends in relative scattered intensity of a sphere in free space as functions of diameter, *d,* and wavelength, λ.

$d < 5$ nm may have a size-dependent index of refraction [5]. The λ^{-4} trend pictured in Fig. 1 would be altered significantly due to the variations in the optical constants as pictured in Fig. 2. This figure shows the wavelength dependence of the optical constants *n, k* for four materials in use for semiconductor manufacturing: crystalline Si (Si-c) [6], amorphous Si (Si-a) [7], hafnium oxide (HfO_2) [8-10], and silicon dioxide (SiO_2) [11]. Third, Eqn. 1 is defined for a sphere in free space, and this simple system cannot account for the complex interactions among the defect, the patterned layout, and the substrate.

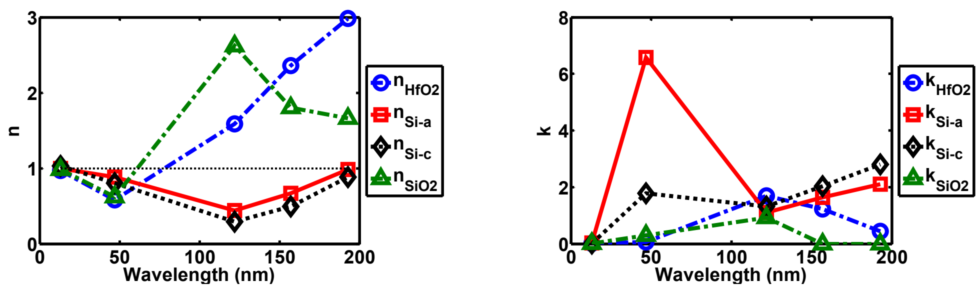

Figure 2. Optical constants *n* and *k* for four key materials used in semiconductor manufacturing, as found in the literature.

Unlike for defect size, this equation cannot be considered as a heuristic model for the effects of wavelength scaling. To develop a fundamental understanding of the effects of reduced wavelength, electromagnetic simulations with realistic patterned layouts and defects are required to determine the qualitative and quantitative effects of reduced wavelengths upon defect inspection. In this paper, a simulation study is presented comparing defect scattering at five different wavelengths using an in-house developed finite-difference time-domain (FDTD) [12] Maxwell's equations solver. A defect metric is developed that is applicable across these five wavelengths. This signal-to-noise based metric will allow direct comparisons of the fundamental performance across these wavelengths and will illustrate the potential gains and challenges of using shorter wavelengths.

2. SIMULATION METHODOLOGY

2.1 Shared geometric simulation inputs

Individual FDTD calculations simulate a single plane wave incident upon the sample with polar and azimuthal angles defined as illustrated in Fig. 3(a). The Cartesian coordinate system is tied to the orientation of the layout as illustrated in that same panel. Simulations are performed with the plane wave linearly polarized either perpendicular to or within the plane of incidence, and these results are used to calculate the effects of linearly polarized light that is oriented with respect to the sample (e.g., X polarization, Y polarization). The simulation geometries are based upon public information about recent manufacturing processes [13, 14] while reducing dimensions such that silicon lines are 8 nm; areas and heights are scaled accordingly. The nominal patterning for all simulations is of Si fins with conformal side coatings and a significant layer of silicon oxide between these fins that is also coated. The four materials used are identified in Fig, 3(b) in the *xz* cross-sectional view, the optical constants for these materials appear as Fig. 2, and the five wavelengths are shown at right in Fig. 1. Figure 3(c) shows the *xy* view of the unit cell (UC) used for this simulation study. Calculations were performed for three cases: first, with no defects in the simulation domain; second, with one bridging defect that connects the ends of two fins together; and third, with one bridging defect that connected

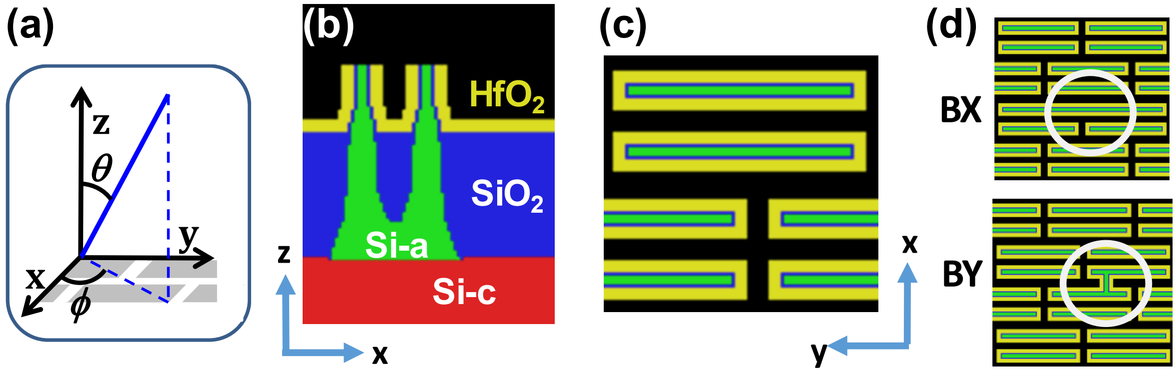

Figure 3. (a) Coordinate system for simulated incident plane wave linear polarization axis and angle of incidence, both polar θ, and azimuthal, ϕ. (b) *yz* cross-section of fin pair modeled upon a transmission electron micrograph in Ref. [14]. Materials shown were chosen from analysis of the public literature. (c) *xy* cross-section through the fins. Image is of one unit cell (UC). (d) *xy* cross-sections showing bridge defects "Bx" and "By" within a 2 UC × 2 UC area. Note, the length of the "Bx" bridge runs along the *y* direction in our coordinate system, and the length of "By" runs along the *x* direction.

adjacent lines together. These bridging defects are commonly referred to by their SEMATECH[1] naming scheme, "Bx" and "By" defects, and are illustrated in Fig. 3(d).

2.2 Essential variations specific to multi-wavelength defect modeling

As in previous reports from our group on the simulations of defect structures using FDTD [2, 15, 16], the patterned structures have been treated as periodic for the purposes of calculation. For these simulations, there is a periodicity in the *xy* directions and perfectly matching layers (PMLs) are placed only at the bottom and top of the simulation domain. As the size of the unit cell in Fig. 3(c) is 168 nm × 180 nm, the placement of one unit cell (UC) containing a defect in the simulation domain is insufficient to model a single defect. There will be defect-dependent interactions with the defect's multiple periodic copies. Therefore, the single defect UC is placed with an array of non-defect UCs as illustrated in Fig. 4.

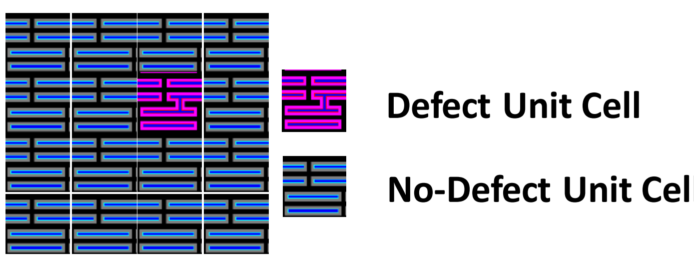

Figure 4. For λ = 13 nm, the simulation domain was populated with by a 4 x 4 array of unit cells (UC) as defined in Fig. 2(c), with only one UC containing a defect to guarantee at least 10 λ separation between the edges of the simulation domain. Domain sizes as functions of wavelength are provided in Table 1.

The *xy* dimensions of the simulation domain determine the lengths between the periodic copies of the "isolated" defect. To ensure a minimal amount of interaction among these copies, our convergence testing (not shown) has determined that this distance should be at least 10 λ, and therefore in performing a multi-wavelength study, the domain size must be relatively large for the longest wavelength can be made smaller for shorter wavelengths. The simulation domain lengths and widths for these five wavelengths are provided in Table 1 in nanometers, in wavelengths, and in unit cells.

[1] Certain commercial materials are identified in this paper in order to specify the experimental procedure adequately. Such identification is not intended to imply recommendation or endorsement by the National Institute of Standards and Technology, nor is it intended to imply that the materials are necessarily the best available for the purpose.

Table 1. FDTD domain size, cubic grid size, and numerical precision as functions of wavelength. Cubic grid size corresponds to the length of one side of a cube used in the simulations, with Δs=2 nm leading to a cube 8 nm^3 in volume. Single precision and double precision are common, alternative names for 32 bytes and 64 bytes, respectively.

λ	**Domain Size**								**Grid Size**	**Floating Point**
	Length			**Width**			**Height**		**Δs**	**Precision**
(nm)	**(UC)**	**(nm)**	**(λ)**	**(UC)**	**(nm)**	**(λ)**	**(nm)**	**(λ)**	**(nm)**	**(bytes)**
13	4	672	51.7	4	720	55.4	300	23.1	1	64
47	8	1344	28.6	8	1440	30.6	300	6.4	2	64
122	8	1344	11.0	7	1260	10.3	300	2.5	2	32
157	10	1680	10.7	9	1800	11.5	300	1.9	2	32
193	12	2016	10.4	11	1980	10.3	300	1.6	2	32

Another essential element of this FDTD simulation work is the wavelength dependence of the cubic grid size, Δs. The in-house FDTD code utilizes a uniform cubic grid size throughout the simulation domain. Convergence testing (not shown) and computational constraints were considered in establishing the grid size. It was confirmed that the cubic grid size could not be less than $\lambda/10$. As will be shown in the following section, the scattered intensities from the 13 nm wavelength simulations can be much lower than that of the other wavelengths. To better enable convergence to a steady-state solution, the FDTD code was operated with a floating-point data type that is 64 bytes long for extreme ultra-violet (EUV) wavelengths, 13 nm and 47 nm, while longer wavelengths were calculated using a 32-byte long floating-point data type. The lower precision allows for an improvement in calculation speed by a factor of four to eight when applicable; limited comparisons between 32-byte and 64-byte simulations for the longer wavelengths, not shown, yielded negligible differences.

2.3 Simulation study parameters

The following section will describe the data processing steps applied to the FDTD outputs after the defect simulations, illustrated using one example from the simulation study. The full set of simulation study parameters that were varied were the type of defect (none, "Bx", or "By"), the linear polarization (X or Y), the incident polar and azimuthal angles, and the incident wavelength. Calculations were performed at as many as thirteen angles for each combination of wavelength, polarization, and defect type, as presented in Section 4.

3. DATA PROCESSING METHODOLOGY

Several data processing steps are required to move from the computationally expensive electromagnetic simulations to a proper quantification of the impact of these parameters upon defect detectability. To better illustrate these procedures, one example comparison at these five wavelengths is presented in this section. This comparison follows the treatment for a single combination of incident angle, linear polarization, and defect type. Specifically, a "By" bridging defect illuminated at normal incidence with X polarization is shown.

3.1 Imaging and differential imaging examples

As noted in the Introduction, each of these five wavelengths can have optical source strengths that can differ greatly in photon flux. Other variations include the applicability and quality of the optical elements. For example, refractive elements are not available below 122 nm thus reflective elements dominate work in the EUV. This study acknowledges that substantive differences exist today for microscopes at shorter wavelengths, but this work concentrates on the fundamental scattering capabilities of these structures for enhancing defect detection as a function of wavelength. Therefore, imaging of the scattered fields from the ideal patterned structure and those containing defects is performed assuming ideal Fourier optics with a large collection numerical aperture of 0.95 NA. Figure 5 shows side-by-side comparisons of the images of the simulation domain with a "By" bridge defect along with the differential image formed by subtracting the no-defect image from the image with the defect. Qualitatively, these data demonstrate an increase in defect-based scattering intensity as the wavelength decreases to 47 nm, but poor intensities at 13 nm. This trend is not unexpected, as 13 nm reflects poorly at normal incidence for many materials.

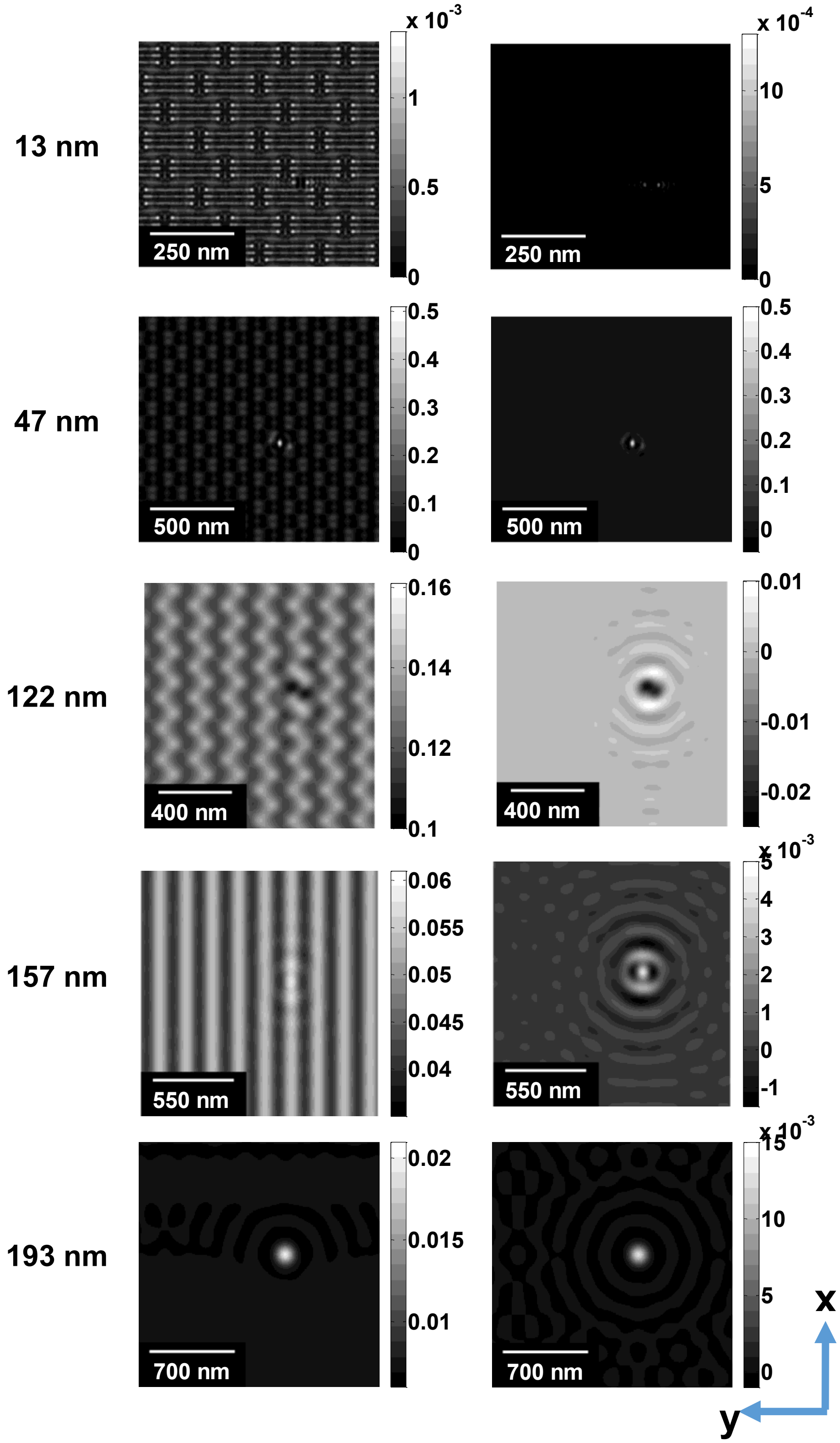

Figure 5. (left) Simulated images and (right) differential images of a "By" bridging defect assuming X polarization and plane wave illumination at normal incidence (θ, ϕ) = (0°, 0°). Differential images are formed by subtracting a no-defect simulated image with the same polarization and incident angle from the simulated image containing the defect. Images at λ = 13 nm are resolved. Higher scattering frequencies exist for 47 nm through 157 nm, while only the defect scattering exceeds the DC component at 193 nm.

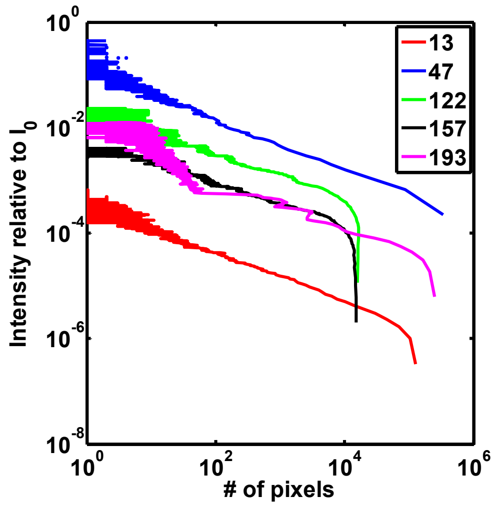

Figure 6. Differential image intensity as a function of the number of pixels in the differential image. Data were obtained by converting each differential image in Fig. 5 to its absolute value and then taking a histogram of the absolute value differential image (AVDI) using 300 bins that evenly divided the full intensity range of each AVDI. The weakest signal appears for the 13 nm AVDI, the strongest for the 47 nm AVDI.

The intensity ranges of the five differential images in Fig. 5 vary greatly with wavelength. The simplest analysis is to compare the peak intensity against zero intensity or the peak-to-valley intensity range, but these rely on one or two pixels out of an image with thousands of pixels. One method for visualizing the scattering variation using all the pixels in these images with wavelength is shown in Fig. 6. Here, the intensity distributions of the absolute value of the differential images (AVDI) are plotted with respect to the number of pixels in the image detecting such an intensity. These data are acquired from performing a binning of the pixels in the AVDI (e.g., a histogram). Figure 6 shows that there are very large numbers of pixels in each of these AVDI that show little to no practical intensity difference due to the defect, or stated more simply no "defect signal". Likewise, there is a relatively small number of pixels that exhibit a relatively strong defect signal.

Notable comparisons in Fig. 6 are among the intensity ranges captured by 100 pixels or less, which are the strongest indicators of the presence of a defect in the AVDI. While the intensity distribution for 193 nm straddles portions of the distribution of 122 nm (and to a lesser extent, 157 nm), there is a clear ordering in these intensity distributions with respect to wavelength. The most sensitive wavelength is 47 nm, followed by 122 nm, 193 nm, and 157 nm, with 13 nm the least sensitive to the "By" defect using X polarization at normal incidence. The intensity differences between the 47 nm response and the 13 nm response are about three orders-of-magnitude for these conditions.

3.2 Applying noise

The data above are presented without the addition of noise sources. The most thorough analysis of simulated defect images requires the inclusion of realistic noise sources. It is preferable to incorporate known sources of wafer noise such as line edge roughness (LER) into the modeling itself, which falls outside the scope of this paper. In addition, the analysis is aided by the proper treatment of process noise, but public information on process noise is lacking. While detectors are vulnerable to a variety of noise sources (e.g., thermal), one noise source is of particular interest for detectors with low photon flux, their inherent Poisson noise. One can make an estimate of the Poisson noise, also known as shot noise, at the detector, which depends upon the number of photons per pixel at the sensor (e.g., charge-coupled device (CCD) camera). The fullest treatment of Poisson noise would be wavelength-dependent, as the various sources have different photon fluxes. A credible lower bound can be established however from estimating the photon flux of a 13 nm wavelength source. Wojdyla *et al.* have reported a value of 64 photons per pixel per exposure in their actinic EUV mask metrology [17]. Conservatively estimating that the signal measured might have been on the order of 1 %, the incident intensity, I_0, may be approximated as 6400 photons per pixel. This value was applied to the determination of the Poisson noise for each individual pixel. In Fig. 7, the noise for the 13 nm wavelength image has a Poisson distribution as the scattering intensities are relatively small. On the other hand, the noise distribution for the 47 nm wavelength image is Gaussian, as Poisson noise has a Gaussian distribution for large photon count values.

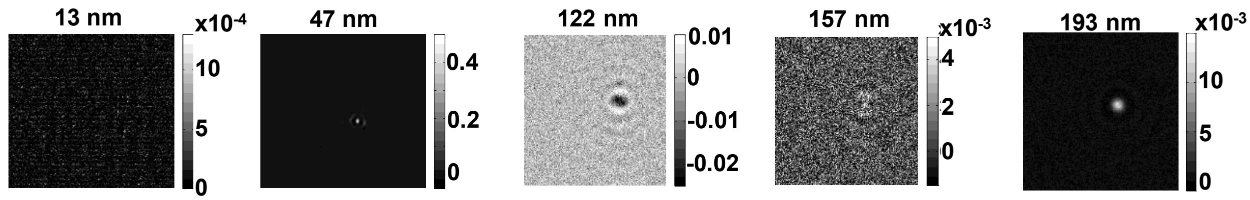

Figure 7. Differential images after the application of Poisson noise, also called shot noise, on both the "By" defect image and the no-defect image for each wavelength.

From Fig. 7, the defect is readily obscured for the 13 nm wavelength and the 157 nm wavelength defect is somewhat suppressed as well.

3.3 Multi-wavelength defect metric

The goal of the study is to quantify the defect detectability as functions of incident angle, polarization, defect type, and wavelength. Thus, a defect metric is required that is applicable across the five wavelengths that is independent of domain size and cubic grid size. Utilizing the absolute value of the differential image (AVDI), an ideal candidate for this defect metric is a signal to noise ratio, defined here as

$$SNR = \frac{I_{signal}}{\sigma_{noise}}, \tag{3}$$

where I_{signal} corresponds to the total intensity gathered due to the defect while σ_{noise} is the standard deviation of the intensities at all pixels falling below certain thresholds; the latter is not to be confused with σ, the standard deviation of the ADVI, as it is a 5σ threshold is initially used to differentiate the pixels with large intensities due to the defect from those pixels with a smaller signal from the defect or the applied noise. In Fig. 8, two examples are provided which illustrate the process of determining this signal-to-noise ratio. At left in Fig. 8 are images showing only those pixels with intensities greater than 5σ. The upper right panel is from the λ = 47 nm simulation and features three regions of interest, while the lower left panel shows the intensity-thresholded λ = 122 nm image, which yields not only a central optical response from the defect but also several pixels of noise. An area threshold is required to separate this random noise from the defect signal. As the wavelength decreases, one might reasonably expect the optical scattering volume from a sub-resolved object to decrease, but for this study a simple area threshold of A_{min} = 1000 nm^2 was sufficient. The center column of Fig. 8 shows the images after the removal of areas below A_{min}. These remaining pixels, colored in green on the right side of Fig. 8, are averaged to determine I_{signal}. The standard deviation of the

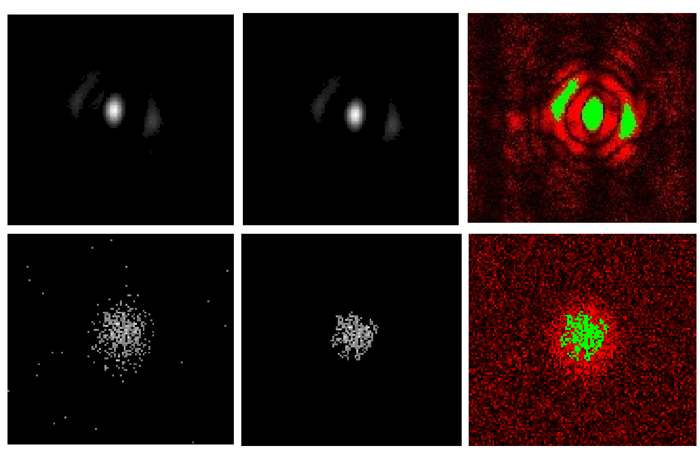

Figure 8. Application of intensity and area thresholding to separate a defect signal from its noise. Top row is data at λ = 47 nm, bottom row is λ = 122 nm. The left column shows pixels with intensities exceeding 5σ. The center column shows the exclusion of areas less than a constant minimum area A_{min}. The right column shows the differential image due to the defect in green with the noise in red, permitting a signal to noise ratio to be determined from a single differential image.

pixel intensities for the pixels in red determines σ_{noise}. For each combination of incident angle, polarization, defect type, and wavelength a signal to noise ratio can be evaluated.

4. SIMULATION STUDY RESULTS

4.1 Comparisons of incident angle using polar plotting

To effectively present the trends in the defect metric data, the SNR is plotted in this paper using polar plotting as illustrated in Fig. 9. In this figure, the SNR at thirteen angles (noted with circles) are shown. Interpolation is made among the points to illustrate the effects of angle-resolved illumination on the defect detectability of the “By” defect using X polarization at $\lambda = 47$ nm. As shown, a polar angle $\theta = 15°$ yields the optimal signal to noise with only a minor difference apparent between $\phi = 30°$ and $\phi = 60°$.

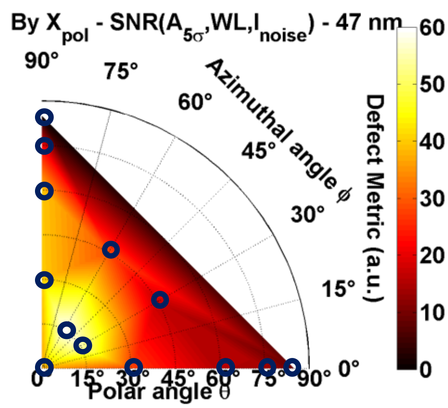

Figure 9. Polar plot of the signal to noise defect metric for the “By” defect illuminated using X-polarized, 47 nm wavelength illumination at 13 angles noted by circles.

4.2 Defect metric results across the five wavelengths

Figures 10 and 11 yield the full results of this simulation study, which yielded over 240 values for the signal to noise defect metric. Each value summarizes a combination of wavelength, defect type, polarization, and incident angle. Each figure is organized as a 2 × 5 array of polar plots to span these combinations.

The clearest observation in this fundamental study is that $\lambda = 47$ nm is the optimal wavelength for defect detection, outperforming $\lambda = 122$ nm by a factor of five or more. Minimal gains are observable decreasing the wavelength from $\lambda = 193$ nm to $\lambda = 122$ nm, but the most pronounced results are from the $\lambda = 47$ nm simulations. Note, the domain size in Table 1 for $\lambda = 47$ nm was relatively large. There were two separate simulations studies at $\lambda = 47$ nm: the first was with a smaller domain and the second with this larger domain to greatly reduce the possibility that these gains are from periodic copies of the defects. These results are independent of these domain sizes.

The lack of appreciable signal at 13 nm should be noted as it was anticipated that larger angles of incidence, that is smaller grazing angles, might have yielded comparable defect detectability. The optical constants $n(\lambda)$ as shown in Fig. 2 are near or at unity at 13 nm, while $k(\lambda)$ is near zero as well at that wavelength. As optical constants for key semiconductor materials are better characterized in the future, additional simulation study may be warranted.

Another observation that has been noted in our prior work is that there is not a single combination of angle of incidence and polarization that is optimal for these defect types. Across the wavelengths, the “Bx” defect in Fig. 10 is better observed using the Y polarization while the “By” defect in Fig. 11 is better detected using X polarization. The bridging directions of these two defects are orthogonal to each other and in both cases, the polarization that optimizes detection runs parallel to the bridging direction of the bridge. There is an azimuthal dependence at $\lambda = 47$ nm for the “Bx” defect with Y polarization, but in general the polar angle seems more important at these wavelengths.

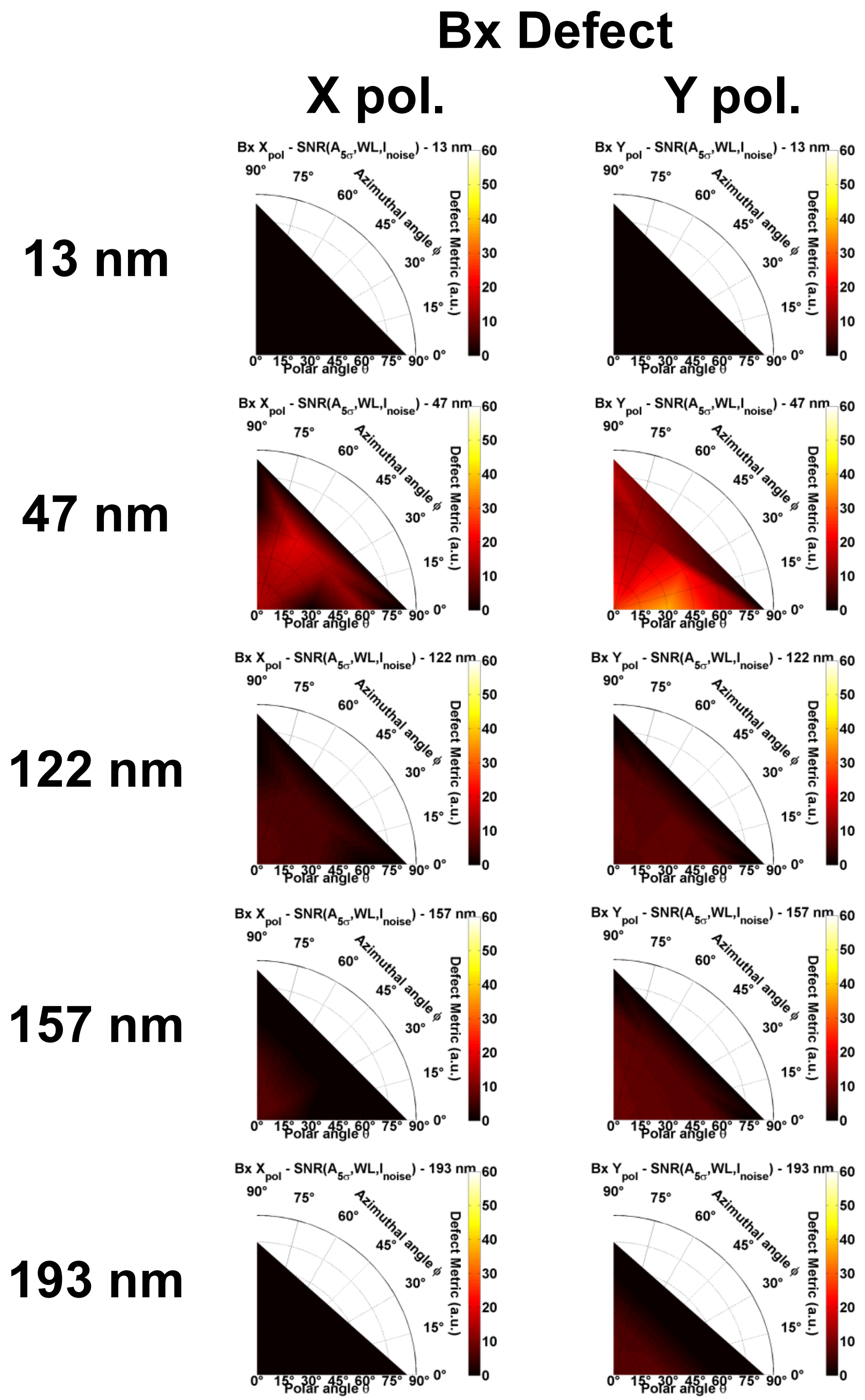

Figure 10. Signal to noise defect metric, plotted in polar plots showing the effects of polar and azimuthal angle, as functions of polarization and wavelength for the "Bx" defect. All plots in Fig. 10 and 11 are on the same color scale. With this defect metric, the $\lambda = 47$ nm yields the greatest defect detectability. Detectability is improved for all wavelengths $\lambda \geq 47$ nm if the linearly polarized illumination is aligned with the direction of the defect.

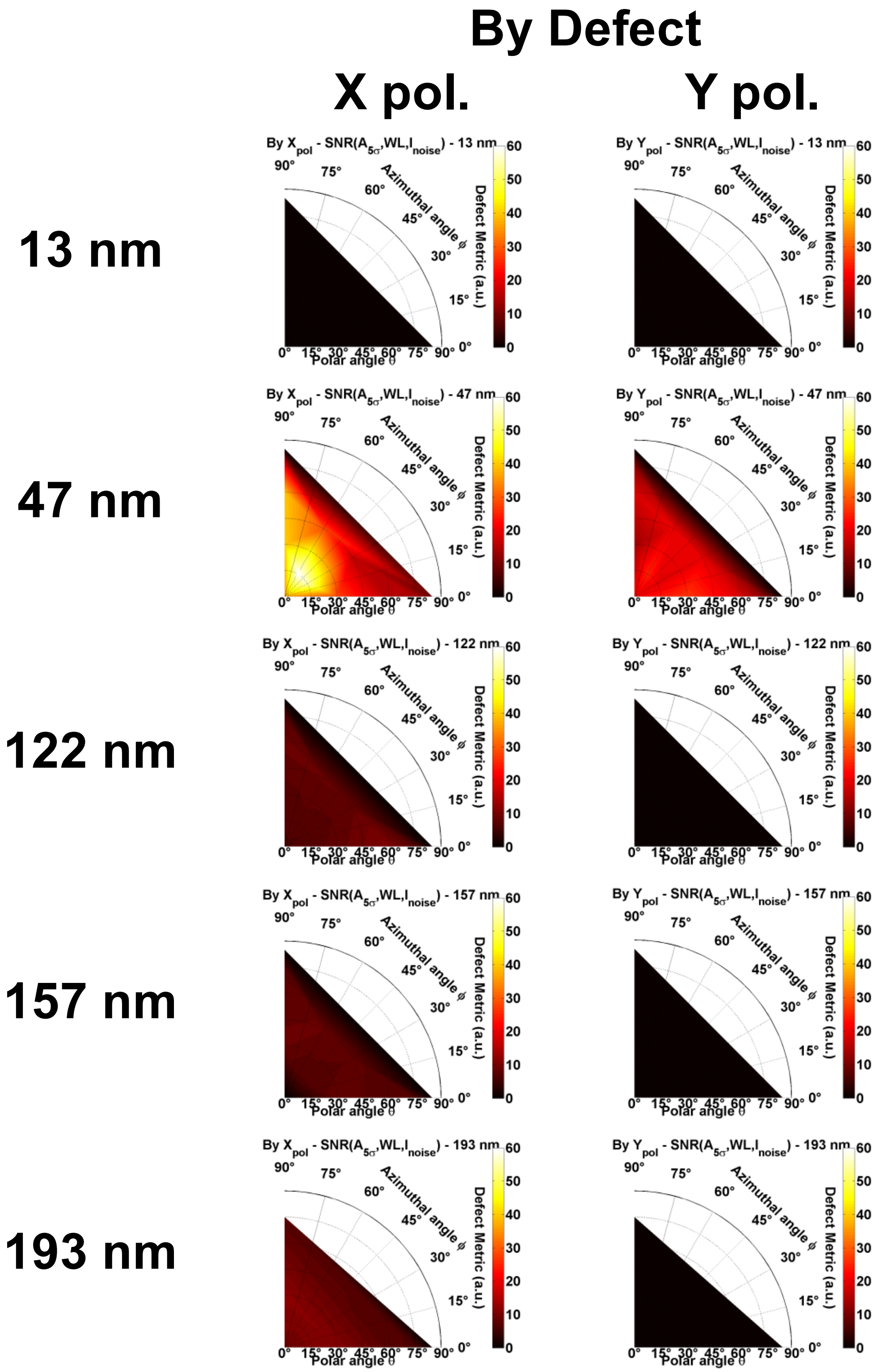

Figure 11. Signal to noise defect metric, plotted in polar plots showing the effects of polar and azimuthal angle, as functions of polarization and wavelength for the "By" defect. All plots in Fig. 10 and 11 are on the same color scale. With this defect metric, the $\lambda = 47$ nm yields the greatest defect detectability. Detectability is improved for all wavelengths $\lambda \geq 47$ nm if the linearly polarized illumination is aligned with the direction of the defect.

5. CONCLUSIONS

A simulation study has been performed at five wavelengths spanning from the DUV, through the VUV, and into the EUV to determine the fundamental improvements in patterned defect detection that may be realized by reducing the inspection wavelength. This study establishes that up to a factor of five improvement may be realized in signal to noise ratio from the adoption of $\lambda = 47$ nm as an inspection wavelength. A shorter EUV wavelength, 13 nm, was ill-suited for defect inspection, yielding differential intensities as much as three orders of magnitude smaller than from simulations using $\lambda = 47$ nm.

These results, based on the basic physics, indicate how defect identification trends with wavelength into the EUV. For example, the optical constants *n* and *k* for 13 nm are at or near 1 and 0, respectively, and a much smaller optical signal is backscattered. The much larger values of *k* at $\lambda = 47$ nm as well as the metallic behavior of *n* at this wavelength contribute to its notably strong response. In addition, the defect is resolved at $\lambda = 13$ nm, thus there is little optical interaction between the scattering due to the defect and the scattering due to the ideal patterned structure. For longer wavelengths, the underlying patterns and defects are unresolved and their scattering interacts, and further work should be performed to define the positive effects of such interactions.

Optimized combinations of incident angle, linear polarization, bridge direction, and wavelength were determined for the two bridge defects. Following the SEMATECH naming scheme, the “Bx” bridge (running along the *y* direction) is enhanced by Y polarization while the “By” bridge (running along the *x* direction) is enhanced by X polarization. This result agrees well with our previous studies of intentional defect arrays at larger critical dimensions.

Although additional work remains to rigorously include the challenges faced at each of these wavelengths, this study reveals the potential gains of reducing the inspection wavelength in patterned defect inspection. To make these results more practical, additional, credible elements need to be considered, such as more process stacks, more materials, available source strengths, microscope configurations, and detector quantum efficiencies and noise.

REFERENCES

[1] C. Hess, and L. H. Weiland, "Issues on the size and outline of killer defects and their influence on yield modeling," IEEE/SEMI 1996 Advanced Semiconductor Manufacturing Conference and Workshop. 423-428 (1996). http://dx.doi.org/10.1109/ASMC.1996.558102

[2] R. M. Silver, B. M. Barnes, Y. Sohn *et al.*, “The Limits and Extensibility of Optical Patterned Defect Inspection,” Proc. SPIE*,* 7638, 76380J (2010). http://dx.doi.org/10.1117/12.850935

[3] T. F. Crimmins, “Defect metrology challenges at the 11nm node and beyond,” Proc. SPIE*,* 7638, 76380H (2010). http://dx.doi.org/10.1117/12.846623

[4] M. I. Mishchenko, “Gustav Mie and the fundamental concept of electromagnetic scattering by particles: A perspective,” J. of Quant. Spectro. Rad. Trans.*,* 110(14–16), 1210-1222 (2009). http://dx.doi.org/10.1016/j.jqsrt.2009.02.002

[5] M. Tian, M. Li, and J. C. Li, “Effect of size on dielectric constant for low dimension materials,” Physica B: Condensed Matter*,* 406(3), 541-544 (2011). http://dx.doi.org/10.1016/j.physb.2010.11.034

[6] D. F. Edwards, [Silicon (Si)*] Academic Press, Boston(1985). http://dx.doi.org/10.1016/B978-0-08-054721-3.50029-0

[7] H. Piller, [Silicon (Amorphous) (a-Si)] Academic Press, Boston(1985). http://dx.doi.org/10.1016/B978-0-08-054721-3.50030-7

[8] D. Franta, D. Nečas, I. Ohlídal *et al.*, “Dispersion model for optical thin films applicable in wide spectral range,” Proc. SPIE*,* 9628, 96281U (2015).

[9] Q.-J. Liu, N.-C. Zhang, F.-S. Liu *et al.*, “Structural, electronic, optical, elastic properties and Born effective charges of monoclinic HfO2 from first-principles calculations,” Chinese Physics B*,* 23(4), 047101 (2014). http://dx.doi.org/10.1088/1674-1056/23/4/047101

[10] E. Filatova, A. Sokolov, J.-M. André *et al.*, “Optical constants of crystalline HfO_2 for energy range 140–930 eV,” Appl. Opt.*,* 49(14), 2539-2546 (2010). http://dx.doi.org/10.1364/AO.49.002539

[11] H. R. Philipp, [Silicon Dioxide (SiO_2), Type α (Crystalline)] Academic Press, Boston(1985). http://dx.doi.org/10.1016/B978-0-08-054721-3.50039-3

[12] A. Taflove, “Application of the Finite-Difference Time-Domain Method to Sinusoidal Steady-State Electromagnetic-Penetration Problems,” IEEE T. Electromag. Compat., EMC-22(3), 191-202 (1980). http://dx.doi.org/10.1109/TEMC.1980.303879

[13] A. Raghunathan, S. Bennett, H. O. Stamper *et al.*, “13nm gate Intentional Defect Array (IDA) wafer patterning by e-beam lithography for defect metrology evaluation,” Microelec. Engr., 88(8), 2729-2731 (2011). http://dx.doi.org/10.1016/j.mee.2011.02.109

[14] S. Natarajan, M. Agostinelli, S. Akbar *et al.*, "A 14nm logic technology featuring 2nd-generation FinFET, air-gapped interconnects, self-aligned double patterning and a 0.0588 μm^2 SRAM cell size." 3.7.1-3.7.3 (2014). http://dx.doi.org/10.1109/IEDM.2014.7046976

[15] B. M. Barnes, F. Goasmat, M. Y. Sohn *et al.*, “Enhancing 9 nm Node Dense Patterned Defect Optical Inspection using Polarization, Angle, and Focus,” Proc. SPIE, 8681, (2013). http://dx.doi.org/10.1117/12.2012250

[16] B. M. Barnes, F. Goasmat, M. Y. Sohn *et al.*, “Effects of wafer noise on the detection of 20-nm defects using optical volumetric inspection,” J. Micro-Nanolitho. MEMS MOEMS, 14(1), 9 (2015). http://dx.doi.org/10.1117/1.jmm.14.1.014001

[17] A. Wojdyla, A. Donoghue, M. P. Benk *et al.*, “Aerial imaging study of the mask-induced line-width roughness of EUV lithography masks,” Proc. SPIE, 9776, 97760H (2016). http://dx.doi.org/10.1117/12.2219513